

# Optimal control in large open quantum systems – the case of transmon readout and reset

Ronan Gautier,<sup>1,2,3</sup> Élie Genois,<sup>1</sup> and Alexandre Blais<sup>1,4</sup>

<sup>1</sup>*Institut Quantique and Département de Physique,  
Université de Sherbrooke, Sherbrooke, QC, Canada*

<sup>2</sup>*Laboratoire de Physique de l'École Normale Supérieure, Inria, ENS,  
Mines ParisTech, Université PSL, Sorbonne Université, Paris, France*

<sup>3</sup>*Alice & Bob, Paris, France*

<sup>4</sup>*Canadian Institute for Advanced Research, Toronto, ON, Canada*

We present a framework that combines the adjoint state method together with reverse-time back-propagation to solve otherwise prohibitively large open-system quantum control problems. Our approach enables the optimization of arbitrary cost functions with fully general controls applied on large open quantum systems described by a Lindblad master equation. It is scalable, computationally efficient, and has a low memory footprint. We apply this framework to optimize two inherently dissipative operations in superconducting qubits which lag behind in terms of fidelity and duration compared to other unitary operations: the dispersive readout and all-microwave reset of a transmon qubit. Our results show that, given a fixed set of system parameters, shaping the control pulses can yield 2x improvements in the fidelity and duration for both of these operations compared to standard strategies. Our approach can readily be applied to optimize quantum controls in a vast range of applications such as reservoir engineering, autonomous quantum error correction, and leakage-reduction units.

*Introduction.*— Quantum optimal control (QOC) provides a framework to design external controls for realizing arbitrary quantum operations with maximal fidelity and minimal time [1–3], crucial requirements of useful quantum error correction [4]. In most practical QOC applications, like the preparation of complex quantum states [5–7], or the design of fast, high-fidelity quantum gates [8–11], only closed-system quantum dynamics are considered. This simplification relies on the assumption that minimizing operation time will also reduce the impact of environmental noise. However, these approaches are limited by the fact that controlling the system’s coherent dynamics can drastically alter the impact of some noise sources, as exemplified by dynamical decoupling methods [12–14]. Moreover, closed-system approaches cannot extend to inherently dissipative processes such as qubit readout and reset. Consequently, optimally controlling open quantum systems emerges as an important avenue [15, 16]. It addresses both the minimization of decoherence in quantum information processing [17–19] and the design of dissipative protocols [20, 21], marking a significant step towards comprehensive quantum control in engineered systems.

Over the last decade, several approaches have emerged for open-system QOC. Methods like Krotov [22] and gradient-ascent pulse engineering (GRAPE) [23, 24] were generalized to include dissipation [21, 25] but stay limited to unitary problems. Closed-loop control methods based on feedback engineering [26, 27] or reinforcement learning [28–31] have seen recent success but fall short in scaling to large numbers of parameters. Automatic differentiation [32–35] fulfills most QOC framework requirements, but suffers from substantial memory demands even for moderate system sizes and evolution times [36].

In this Letter, we present a framework enabling the re-

alization of QOC on large open quantum systems with a fully general parametrization over the controls and arbitrarily complex cost functions. Our approach combines the adjoint state method [37–39] with reverse-time back-propagation [40–44] to solve otherwise prohibitive open-system quantum control problems defined in Lindblad form. This approach ensures precise and fast numerical computation of arbitrary gradients with minimal memory usage, making it ideal for GPU acceleration. In the second part of this work, we demonstrate the usefulness of this approach by optimizing two critical operations for the realization of a fault-tolerant quantum computer based on superconducting circuits: dispersive readout [45–47] and all-microwave reset [48, 49] of a transmon qubit [50].

*Adjoint state method.*— Consider a QOC problem for which we seek to find a set of parameters minimizing a cost function  $C(\theta, \hat{\rho}(t_0), \dots, \hat{\rho}(t_n))$ . This function, in general, depends on both the problem parameters  $\theta = (\theta_1, \dots, \theta_m)$  and on the density matrix of the system at a set of times,  $\hat{\rho}(t_i)$ . Gradient-based approaches to optimize the control parameters rely on computing the derivative of the cost function with respect to each parameter,  $dC/d\theta$ . To do so, we apply the adjoint state method [37] to open quantum systems. In this context, the adjoint state is defined as  $\hat{\phi}(t) = dC/d\hat{\rho}(t)$ , and represents how a change in the density matrix at time  $t$  modifies the cost function. For open quantum systems under the usual Born-Markov approximations [51], the evolution of the density matrix is governed by a Lindblad master equation ( $\hbar = 1$ ),

$$\frac{d\hat{\rho}}{dt} = \mathcal{L}\hat{\rho} \equiv -i[\hat{H}, \hat{\rho}] + \sum_k \mathcal{D}[\hat{L}_k]\hat{\rho}, \quad (1)$$

where  $\hat{H}$  is the system Hamiltonian,  $\hat{L}_k$  are jump operators, and  $\mathcal{D}[\hat{L}]\hat{\rho} = \hat{L}\hat{\rho}\hat{L}^\dagger - \{\hat{L}^\dagger\hat{L}, \hat{\rho}\}/2$ . The adjoint state is then subject to a dual ordinary differential equation [52],

$$\frac{d\hat{\phi}}{dt} = -\mathcal{L}^\dagger\hat{\phi} \equiv -i[\hat{H}, \hat{\phi}] - \sum_k \mathcal{D}^\dagger[\hat{L}_k]\hat{\phi}, \quad (2)$$

where  $\mathcal{D}^\dagger[\hat{L}]\hat{\phi} = \hat{L}^\dagger\hat{\phi}\hat{L} - \{\hat{L}^\dagger\hat{L}, \hat{\phi}\}/2$ . This equation can be integrated numerically over the time interval of interest  $[t_0, t_n]$  with initial condition  $\hat{\phi}(t_n) = \partial C/\partial\hat{\rho}(t_n)$ , computed analytically if a closed form is available, or directly through automatic differentiation. Notably, the overall minus sign in Eq. (2) ensures numerical stability of the integration by generating contracting dynamics in reverse time. The derivative of the cost function with respect to the problem parameters is given by

$$\frac{dC}{d\theta} = \frac{\partial C}{\partial\theta} - \int_{t_n}^{t_0} \partial_\theta \text{Tr}[\hat{\phi}^\dagger(t)\mathcal{L}(t, \theta)\hat{\rho}(t)] dt. \quad (3)$$

This integral is straightforward to compute using the density matrix and adjoint state at each time  $t \in [t_0, t_n]$ , as obtained from Eqs. (1) and (2). In particular, the partial derivative with respect to  $\theta$  can be easily computed from automatic differentiation of the adjoint state equation by noting that

$$\partial_\theta \text{Tr}[\hat{\phi}^\dagger\mathcal{L}\hat{\rho}] = -\text{Tr}[\partial_\theta(d\hat{\phi}/dt)^\dagger\hat{\rho}], \quad (4)$$

which has the form of a vector-Jacobian product.

The QOC optimization is illustrated in Fig. 1 and proceeds in two steps. First, the forward pass consists in using the initial set of parameters (e.g. a sequence of discrete pulses) to numerically integrate the master equation from  $t_0$  to  $t_n$  while saving the density matrix at each time  $t_i$  of interest. The cost function  $C(\theta, \hat{\rho}(t_0), \dots, \hat{\rho}(t_n))$  is then evaluated. To lower the memory footprint, the cost function can also be evaluated on the fly during the forward pass such that only a single density matrix needs to be stored. In a second step, the backward pass, both the master and adjoint equations are simultaneously integrated in reverse time, starting from  $t = t_n$ . During this process, the integral of Eq. (3) is iteratively evaluated, such as to obtain the entire gradients  $dC/d\theta$  once the backpropagation is finished. Having access to the gradients of the cost function, we can now iteratively update the control parameters using standard optimization algorithms [53–55].

We emphasize how each density matrix (blue) is computed twice: once during the forward pass, and once during the backward pass. This enables a low memory footprint for the overall scheme, with at most a single density matrix and adjoint state needed to be stored at any given moment. The memory footprint of the method thus scales as  $\mathcal{O}(N^2)$  with  $N$  the Hilbert space dimension. This is in stark contrast with methods based on

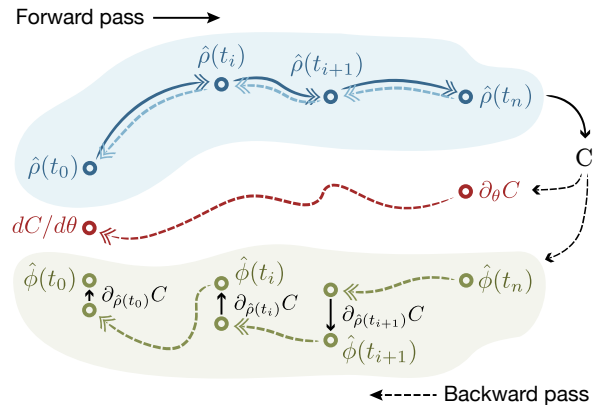


Figure 1. Adjoint state quantum optimal control. In the forward pass, the master equation is integrated and checkpointed for several time points (dark blue). In the backward pass, the density matrix  $\hat{\rho}$  is recomputed in reverse time (light blue) together with the adjoint state  $\hat{\phi}$  (green) and with the gradients (red) of the cost function  $C$ . When a checkpoint is reached, the density matrix is restored to its forward time trajectory, and the adjoint state updated with the corresponding cost function gradient.

automatic differentiation [33], for which the density matrix needs to be stored at each time point of the numerical integration, thus scaling as  $\mathcal{O}(M_t N^2)$ , with  $M_t$  the number of numerical integration steps. Such memory requirements can quickly become prohibitive, even for open quantum systems of intermediate sizes,  $N \gtrsim 100$ .

Note that this large gain in memory comes at the cost of trading off some numerical runtime. Overall, the scheme requires the integration of four differential equations in total [52], against only two for automatic differentiation. In addition, the reverse time integration of Eq. (1) can be numerically unstable due to the expansive dynamics of the system. This can however be fully resolved with checkpointing the quantum states during the forward pass [44], thus effectively trading back some memory for numerical stability. In practice, checkpointing at the time scale of the largest dissipation operator is sufficient to ensure numerical stability without adding significant complexity.

We have implemented this optimization scheme using PyTorch [56], taking advantage of its automatic differentiation capabilities and GPU support. This framework allows us to run optimization problems for open quantum system with hundreds of parameters, arbitrary cost functions, and for Hilbert space dimensions of up to  $N \sim 5000$  while running on a single GPU with 24 GB of memory. Our code is available through the `dynamics` open-source library [57], simplifying replication of this work and its application to various QOC problems. We now demonstrate the usefulness of this method by optimizing readout and reset of a transmon, two operations that inherently rely on dissipation.

*Transmon model.*— Let us consider the experimentally realistic model depicted in Fig. 2(a) of a transmon

coupled to a readout resonator and Purcell filter [58]

$$\frac{d\hat{\rho}}{dt} = -i[\hat{H}, \hat{\rho}] + \gamma\mathcal{D}[\hat{b}]\hat{\rho} + \kappa\mathcal{D}[\hat{f}]\hat{\rho}, \quad (5)$$

with transmon relaxation rate  $\gamma$  and filter relaxation rate  $\kappa$ , and where

$$\begin{aligned} \hat{H} = & 4E_C\hat{n}_t - E_J\cos(\hat{\varphi}_t) + \omega_r\hat{a}^\dagger\hat{a} + \omega_f\hat{f}^\dagger\hat{f} \\ & - ig\hat{n}_t(\hat{a} - \hat{a}^\dagger) - J(\hat{a} - \hat{a}^\dagger)(\hat{f} - \hat{f}^\dagger) \\ & + \Omega_t\hat{n}_t\sin(\omega_{d,t}t) - i\Omega_f(\hat{f} - \hat{f}^\dagger)\sin(\omega_{d,f}t). \end{aligned} \quad (6)$$

The first two terms denote the free transmon Hamiltonian with charging energy  $E_C$  and Josephson energy  $E_J$ , with  $\hat{n}_t$  and  $\hat{\varphi}_t$  the charge and phase operators, and with  $\hat{b}$  the corresponding annihilation operator in the diagonal basis. The resonator and filter modes are denoted by  $\hat{a}$  and  $\hat{f}$ , with respective frequencies  $\omega_r$  and  $\omega_f$ . These three modes are capacitively coupled in series with coupling strengths  $g \gg J$ . The system can be driven using a capacitive coupling either through the transmon with a microwave pulse at frequency  $\omega_{d,t}$  and envelope  $\Omega_t(t)$ , or through the Purcell filter at frequency  $\omega_{d,f}$  and envelope  $\Omega_f(t)$ .

For numerical simulation of this model, we first diagonalize the free transmon Hamiltonian and identify the lowest energy eigenstates. We also diagonalize the resonator-filter subsystem yielding two normal modes, each coupled to the transmon. Finally, we apply the rotating-wave approximation (RWA) on couplings and drives. This allows for larger numerical time steps by eliminating fast oscillating dynamics thereby simplifying master equation integration. However, this also implies that not all of the chaotic or transmon ionization dynamics are captured [59–61]. To avoid probing these regimes, we limit the maximum amplitudes of control drives, e.g. to 200 MHz for transmon readout.

Unless stated otherwise, we use  $E_C/2\pi = 315$  MHz,  $E_J/E_C = 51$ , corresponding to a bare transmon frequency  $\omega_t/2\pi = 6$  GHz and to an anharmonicity  $\alpha/2\pi = -349$  MHz. The resonator and filter frequencies are  $\omega_r/2\pi = 7.2$  GHz and  $\omega_f/2\pi = 7.21$  GHz with couplings  $g/2\pi = 150$  MHz and  $J/2\pi = 30$  MHz. This yields a transmon-resonator detuning of  $\Delta/2\pi = 1.2$  GHz, a critical photon number of  $\bar{n}_{\text{crit}} = (\Delta/2g)^2 = 16$  [45] and dispersive rates of  $\chi/2\pi = 3.8$  MHz and 8.1 MHz with the lower and higher normal modes, respectively. Finally, the filter loss rate is  $\kappa/2\pi = 30$  MHz and the transmon relaxation rate is  $\gamma/2\pi = 8$  kHz, i.e.  $T_1 = 20$   $\mu$ s.

*Transmon readout.*— Readout of transmon qubits is realized through the dispersive coupling to a resonator [45]. In this case, the resonator frequency is shifted by the average occupancy in the transmon, and can be measured by driving the resonator at its bare frequency and monitoring the output field, see Fig. 2(b). In the presence of a Purcell filter, either normal mode of the hybridized resonator-filter subsystem can be used for readout [62].

The metric we use to maximize the measurement fidelity is the signal-to-noise ratio (SNR). Accounting for optimal weighting functions, it reads [63]

$$\text{SNR}(\tau_m) = \sqrt{2\eta\kappa \int_0^{\tau_m} dt |\beta_e(t) - \beta_g(t)|^2}, \quad (7)$$

where  $\eta \in [0, 1]$  is the measurement efficiency,  $\tau_m$  is the readout integration time, and  $\beta_{e/g} = \text{Tr}[\hat{f}\hat{\rho}_{g/e}]$  is the average field value in the filter mode, with  $\hat{\rho}_{g/e}$  the density matrix obtained after initializing the transmon in the  $|g/e\rangle$  state. To obtain results that can be compared to experiments, we use  $\eta = 0.6$  [46]. The optimization objective is to maximize the SNR, and thus maximize the distance between the pointer states  $|\beta_e - \beta_g|$  in the shortest possible time. Further assuming that the pointer states  $\beta_{g,e}$  are Gaussian, one can link the SNR and the transmon lifetime to the readout assignment error [52, 62, 64].

To optimize the transmon readout, we discretize the control pulse envelopes  $\Omega(t)$  with 1 ns time bins and use a 250 MHz gaussian filter to interpolate between these pixels during numerical integration and to model realistic experimental distortions [65]. In addition to the discretized drive amplitudes, the optimization parameters  $\theta$  include the carrier frequency  $\omega_d$  of each drive. Contrary to the drive amplitudes, the latter are kept constant throughout the pulse duration, in accordance with typical experiments. The cost function used to optimize the transmon readout is principally composed of the SNR of Eq. (7), with additional cost terms constraining the control pulses in order to regularize the optimization and avoid out-of-model dynamics. For example, we limit the number of photons in the hybridized resonator-filter modes, penalize unwanted transitions to higher excited transmon states, and limit the maximal available pulse amplitudes. The full cost function is detailed in [52]. We perform gradient descent using Adam [54] and use the adjoint state method previously described to compute gradients.

Figure 2(c) shows the SNR and the assignment error as a function of the integration time  $\tau_m$  obtained by our approach, and panel (d) shows the corresponding pulse envelopes for  $\tau_m = 40$  ns optimizations. As a point of comparison, we first consider the two non-optimized reference pulses labelled ‘flat’ and ‘two-step’. The former consists of a constant pulse with 2 ns ramp-up and ramp-down times (dark blue squares), and the latter of a two-step pulse meant to rapidly populate the readout mode (blue circles) [46]. In both cases, the amplitude is calibrated to reach  $\bar{n} = \bar{n}_{\text{crit}}$  photons in the steady state. The SNR versus  $\tau_m$  for these two pulses is fitted with the function (full blue and dark blue lines) [58]

$$\text{SNR}(\tau_m) = \alpha\sqrt{2\eta\kappa}(\sqrt{\tau_m} - \sqrt{\tau_{m,0}}), \quad (8)$$

where  $\alpha = 2|\Omega_f \sin(2\phi)|/\kappa$  is the effective resonator displacement in the steady state, with  $\phi = \arctan(2\chi/\kappa)$  and  $\chi$  the dispersive shift obtained from exact diagonalization of Eq. (6). In this expression,  $\sqrt{\tau_{m,0}}$  accounts for

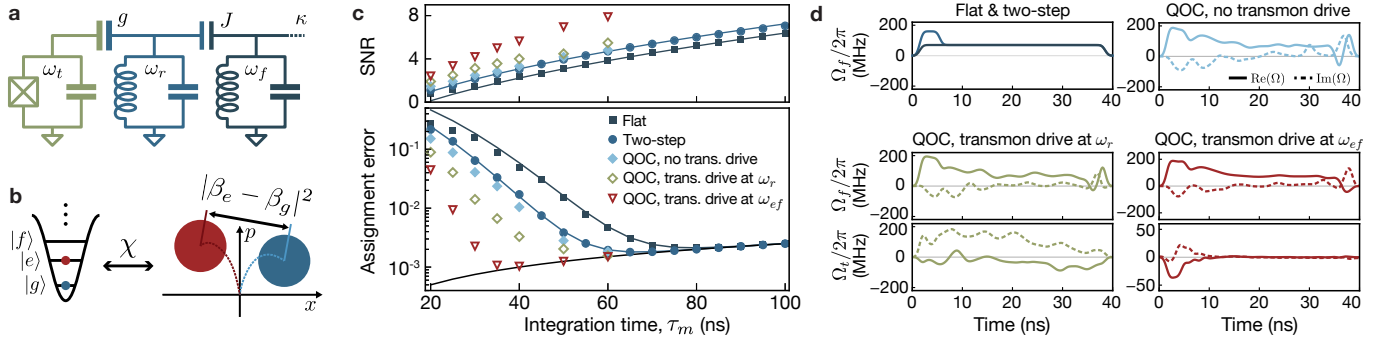


Figure 2. (a) Lumped-element model of a transmon coupled to a readout resonator and Purcell filter. The transmon and filter are driven, and the filter output field is measured through its transmission line. (b) Dispersive readout of a transmon. The mean field in the filter depends on the transmon state. Signal-to-noise ratio of readout increases with the integrated difference of mean fields. (c) Signal-to-noise ratio and assignment error of transmon readout for several drive envelopes: a flat envelope, a 4 ns two-step envelope [46], and optimized envelopes (QOC) with optional additional drives on the transmon at frequencies  $\omega_{d,t} \simeq \omega_r$  (green) and  $\omega_{d,t} \simeq \omega_{ef}$  (red). The flat and two-step data points are fitted according to Eq. (8). The black line shows the  $T_1$  limit given by  $\tau_m/2T_1$ . (d) Reference and optimized pulse envelopes at 40 ns of integration time.

an initial delay for the resonator to populate, and is numerically fitted to  $\tau_{m,0} = 19$  ns and  $\tau_{m,0} = 13$  ns for the flat and two-step pulses, respectively. As the integration time increases, the SNR (assignment error) of both references pulses increase (decrease), up until the transmon  $T_1$  limit is reached (solid black line). Minimum assignment errors of  $2.1 \times 10^{-3}$  and  $1.8 \times 10^{-3}$  are obtained at 80 ns and 65 ns respectively. This is similar performance to state-of-the-art readout experiments [46, 47, 62, 66], as expected from our choice of realistic experimental parameters. Our objective is now to obtain smaller assignment errors in shorter measurement times.

The light blue symbols in Fig. 2(c) are obtained by optimizing the pulse envelope and drive frequency using our QOC approach. The gain is modest and mainly limited by the dispersive coupling with the transmon. Interestingly, the optimized pulses follow a two-step-like shape with a strong initial drive and a weaker subsequent drive, see panel (d). We attribute the small oscillations in the envelope to the rotational gauge freedom of the resonators, which the optimizer is arbitrarily choosing.

Significant improvements are, however, obtained by adding a drive on the transmon concurrently to the readout drive on the resonator. Interestingly, the optimizer converges on two distinct frequencies for the transmon drive. The first strategy found by the optimizer is to drive the transmon at a frequency close to the resonator frequency (green symbols). In that case, the assignment errors decrease faster with integration time than with the above approaches, leading to a minimal assignment error of  $1.6 \times 10^{-3}$  at 60 ns. The effectiveness of this optimized readout strategy stems from the fact that driving the qubit at the resonator frequency creates a longitudinal-like interaction that can be combined with the usual dispersive interaction to improve readout, as demonstrated in Refs. [67–69].

The second strategy found by the optimizer employs a transmon drive at the (ac-Stark shifted)  $|e\rangle$ - $|f\rangle$  transition

frequency (red symbols). Given that the cavity response differs more significantly between the transmon states  $|g\rangle$  and  $|f\rangle$  than between  $|g\rangle$  and  $|e\rangle$  [58], transferring population into the  $|f\rangle$  state leads to a significant improvement of the assignment error, which reaches  $1.0 \times 10^{-3}$  in 40 ns. Interestingly, this shelving approach has already been used to improve readout in circuit QED [70–73]. There, a  $\pi$ -pulse between  $|e\rangle$  and  $|f\rangle$  is applied to the transmon followed by the measurement drive. In contrast, the optimized strategy found here applies the  $\pi$ -pulse while the cavity is loaded with measurement photons leading to a considerable reduction in the measurement time, see Fig. 2(d). This is possible because the optimizer accounts for the time-dependent ac-Stark shift. The optimized  $\pi$ -pulse features a DRAG-like envelope [8] and achieves a gate fidelity over 99 % in less than 10 ns, even while the readout mode is being strongly driven. Importantly, we note that this approach could achieve significantly higher fidelities by increasing the modest transmon lifetime of 20  $\mu$ s used here, as shown by the high SNR in Fig. 2(c).

*Transmon reset.* — As a second demonstration of the adjoint state method, we consider the optimization of the  $f_0$ - $g_1$  reset of a transmon [48, 49, 74]. This is an all-microwave reset protocol based on a Raman transition between states  $|f_00\rangle$  and  $|g_01\rangle$ . For the ket  $|ijk\rangle$ ,  $|i\rangle$  stands for the qubit state and  $|jk\rangle$  the resonator-filter normal modes. Given the large photon loss rate of the filter, the state  $|g_01\rangle$  quickly decays to  $|g_00\rangle$ , thus ensuring a fast reset of the transmon  $|f\rangle$  state. An additional drive at the  $|e\rangle$ - $|f\rangle$  transition frequency allows to reset both  $|e\rangle$  and  $|f\rangle$  states of the transmon. We use the adjoint-state method to find optimal controls for both the  $f_0$ - $g_1$  and  $e$ - $f$  drives simultaneously, in a similar fashion as for optimizing the readout. The cost function is now principally maximizing the transmon population in the  $|g_00\rangle$  state at the end of the protocol, along with smaller contributions for regularizing the pulses, see [52] for details.

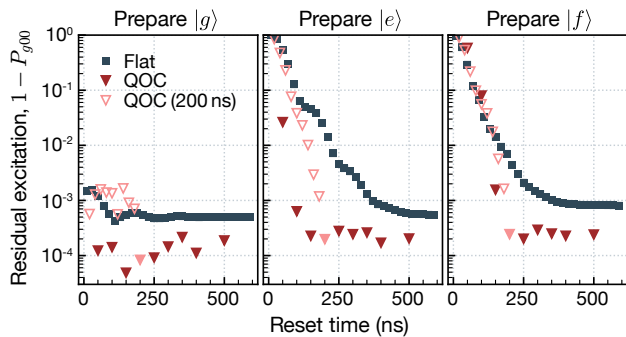


Figure 3. Residual excitation out of  $|g00\rangle$  after  $f0$ - $g1$  reset for a calibrated pulse (blue) and an optimized pulse (red) for a system prepared in  $|g00\rangle$ ,  $|e00\rangle$ , and  $|f00\rangle$ . Each filled red marker corresponds to a different optimization. Lighter hollow markers illustrate the population dynamics at shorter times for the optimized pulse with 200 ns duration.

The results of the reset optimization are summarized in Fig. 3. The three panels show the residual excitation out of  $|g00\rangle$  against the reset time for a reference flat pulse (blue) and an optimized pulse (red) for different initial transmon states. The reference pulse is composed of two constant drives at the  $f0$ - $g1$  and  $e$ - $f$  transitions, where amplitudes and frequencies are calibrated numerically in a similar fashion to what is done in experiments, see [52]. The QOC pulse is obtained by optimizing the carrier frequency and envelopes of both drives, for several total reset times. The optimized pulses show significant improvement over the reference, with a residual excitation of less than 0.05 % at 100 ns (200 ns) for the  $|e\rangle$  ( $|f\rangle$ ) state preparation. Note that this delay in the  $|f\rangle$  reset time is due to a larger relative weight for the reset of  $|e\rangle$  chosen in the cost function, and could be adjusted to achieve the most experimentally relevant reset scheme. This represents a notable improvement over the reference pulses, which reach a steady state after more than 300 ns with larger residual excitations of about 0.07 %. Our results also favourably compare to state-of-the-art experimental realizations of this protocol that reach 1.7 % residual excitations in 100 ns [47], or 0.3 % in 300 ns [49].

*Conclusion.*— We obtained a fully general framework to optimize open quantum system dynamics in large Hilbert spaces by combining the adjoint state method and reverse-time back-propagation. We have demonstrated the applicability of this method to complex open-system optimization problems using the example of superconducting transmon readout and reset. We stress that our method can readily be applied to optimizing a wide range of quantum control problems where the dissipative dynamics play a significant role such as reservoir (dissipation) engineering [75, 76], autonomous QEC [77, 78], leakage-reduction units [79], quantum cooling, and more. We encourage readers to apply this framework on their own optimal control problems using the open-source library `dynamiqs` [57].

*Acknowledgments.*— We sincerely thank Alain Sarlette, Christiane Koch, Ross Shillito, Cristobal Lledó, Pierre Guilmin and Adrien Bocquet for useful discussions. R.G. extends his gratitude to Alain Sarlette for helping organise and support this long-term academic exchange. This work was supported by grant ANR-18-CE47-0005, NSERC, the Canada First Research Excellence Fund, and the Ministère de l'Économie et de l'Innovation du Québec. The numerical simulations were performed using HPC resources at Institut quantique and Inria Paris.

## REFERENCES

- [1] A. P. Peirce, M. A. Dahleh, and H. Rabitz, Optimal control of quantum-mechanical systems: Existence, numerical approximation, and applications, *Phys. Rev. A* **37**, 4950 (1988).
- [2] J. Werschnik and E. Gross, Quantum optimal control theory, *Journal of Physics B: Atomic, Molecular and Optical Physics* **40**, R175 (2007).
- [3] C. P. Koch, U. Boscain, T. Calarco, G. Dirr, S. Filipp, S. J. Glaser, R. Kosloff, S. Montangero, T. Schulte-Herbrüggen, D. Sugny, and F. K. Wilhelm, Quantum optimal control in quantum technologies. strategic report on current status, visions and goals for research in europe, *EPJ Quantum Technology* **9**, 10.1140/epjqt/s40507-022-00138-x (2022).
- [4] B. M. Terhal, Quantum error correction for quantum memories, *Rev. Mod. Phys.* **87**, 307 (2015).
- [5] S. Günther, N. A. Petersson, and J. L. DuBois, Quantum optimal control for pure-state preparation using one initial state, *AVS Quantum Science* **3** (2021).
- [6] V. N. Petruhanov and A. N. Pechen, Optimal control for state preparation in two-qubit open quantum systems driven by coherent and incoherent controls via grape approach, *International Journal of Modern Physics A* **37**, 2243017 (2022).
- [7] W. Cai, Y. Ma, W. Wang, C.-L. Zou, and L. Sun, Bosonic quantum error correction codes in superconducting quantum circuits, *Fundamental Research* **1**, 50–67 (2021).
- [8] F. Motzoi, J. M. Gambetta, P. Rebentrost, and F. K. Wilhelm, Simple pulses for elimination of leakage in weakly nonlinear qubits, *Phys. Rev. Lett.* **103**, 110501 (2009).
- [9] M. H. Goerz, F. Motzoi, K. B. Whaley, and C. P. Koch, Charting the circuit qed design landscape using optimal control theory, *npj Quantum Information* **3**, 37 (2017).
- [10] M. Werninghaus, D. J. Egger, F. Roy, S. Machnes, F. K. Wilhelm, and S. Filipp, Leakage reduction in fast superconducting qubit gates via optimal control, *npj Quantum Information* **7**, 10.1038/s41534-020-00346-2 (2021).
- [11] S. Jandura and G. Pupillo, Time-optimal two- and three-qubit gates for rydberg atoms, *Quantum* **6**, 712 (2022).
- [12] L. Viola, E. Knill, and S. Lloyd, Dynamical decoupling of open quantum systems, *Phys. Rev. Lett.* **82**, 2417 (1999).
- [13] K. Khodjasteh and D. A. Lidar, Fault-tolerant quantum dynamical decoupling, *Phys. Rev. Lett.* **95**, 180501 (2005).
- [14] M. J. Biercuk, H. Uys, A. P. VanDevender, N. Shiga, W. M. Itano, and J. J. Bollinger, Optimized dynamical

- decoupling in a model quantum memory, *Nature* **458**, 996 (2009).
- [15] C. P. Koch, Controlling open quantum systems: tools, achievements, and limitations, *Journal of Physics: Condensed Matter* **28**, 213001 (2016).
- [16] S. Kallush, R. Dann, and R. Kosloff, Controlling the uncontrollable: Quantum control of open-system dynamics, *Science Advances* **8**, eadd0828 (2022).
- [17] M. H. Goerz, D. M. Reich, and C. P. Koch, Optimal control theory for a unitary operation under dissipative evolution, *New Journal of Physics* **16**, 055012 (2014).
- [18] T. Propson, B. E. Jackson, J. Koch, Z. Manchester, and D. I. Schuster, Robust quantum optimal control with trajectory optimization, *Phys. Rev. Appl.* **17**, 014036 (2022).
- [19] Z. An, H.-J. Song, Q.-K. He, and D. L. Zhou, Quantum optimal control of multilevel dissipative quantum systems with reinforcement learning, *Phys. Rev. A* **103**, 012404 (2021).
- [20] D. J. Egger and F. K. Wilhelm, Optimal control of a quantum measurement, *Phys. Rev. A* **90**, 052331 (2014).
- [21] S. Boutin, C. K. Andersen, J. Venkatraman, A. J. Ferris, and A. Blais, Resonator reset in circuit qed by optimal control for large open quantum systems, *Phys. Rev. A* **96**, 042315 (2017).
- [22] V. Krotov, *Global methods in optimal control theory*, Vol. 195 (CRC Press, 1995).
- [23] N. Khaneja, T. Reiss, C. Kehlet, T. Schulte-Herbrüggen, and S. J. Glaser, Optimal control of coupled spin dynamics: design of nmr pulse sequences by gradient ascent algorithms, *Journal of Magnetic Resonance* **172**, 296 (2005).
- [24] T. Schulte-Herbrüggen, A. Spörl, N. Khaneja, and S. Glaser, Optimal control for generating quantum gates in open dissipative systems, *Journal of Physics B: Atomic, Molecular and Optical Physics* **44**, 154013 (2011).
- [25] M. Goerz, D. Basilewitsch, F. Gago-Encinas, M. G. Krauss, K. P. Horn, D. M. Reich, and C. Koch, Krotov: A python implementation of krotov's method for quantum optimal control, *SciPost physics* **7**, 080 (2019).
- [26] H. Chen, H. Li, F. Motzoi, L. Martin, K. B. Whaley, and M. Sarovar, Quantum proportional-integral (pi) control, *New Journal of Physics* **22**, 113014 (2020).
- [27] R. Porotti, V. Peano, and F. Marquardt, Gradient-ascent pulse engineering with feedback, *PRX Quantum* **4**, 030305 (2023).
- [28] V. V. Sivak, A. Eickbusch, H. Liu, B. Royer, I. Tsioutsios, and M. H. Devoret, Model-free quantum control with reinforcement learning, *Phys. Rev. X* **12**, 011059 (2022).
- [29] V. Sivak, A. Eickbusch, B. Royer, S. Singh, I. Tsioutsios, S. Ganjam, A. Miano, B. Brock, A. Ding, L. Frunzio, *et al.*, Real-time quantum error correction beyond break-even, *Nature* **616**, 50–55 (2023).
- [30] Y. Baum, M. Amico, S. Howell, M. Hush, M. Liuzzi, P. Mundada, T. Merkh, A. R. Carvalho, and M. J. Biercuk, Experimental deep reinforcement learning for error-robust gate-set design on a superconducting quantum computer, *PRX Quantum* **2**, 040324 (2021).
- [31] L. Ding, M. Hays, Y. Sung, B. Kannan, J. An, A. Di Paolo, A. H. Karamlou, T. M. Hazard, K. Azar, D. K. Kim, B. M. Niedzielski, A. Melville, M. E. Schwartz, J. L. Yoder, T. P. Orlando, S. Gustavsson, J. A. Grover, K. Serniak, and W. D. Oliver, High-fidelity, frequency-flexible two-qubit fluxonium gates with a transmon coupler, *Phys. Rev. X* **13**, 031035 (2023).
- [32] H. Jirari, Optimal control approach to dynamical suppression of decoherence of a qubit, *Europhysics Letters* **87**, 40003 (2009).
- [33] N. Leung, M. Abdelhafez, J. Koch, and D. Schuster, Speedup for quantum optimal control from automatic differentiation based on graphics processing units, *Phys. Rev. A* **95**, 042318 (2017).
- [34] A. G. Baydin, B. A. Pearlmutter, A. A. Radul, and J. M. Siskind, Automatic differentiation in machine learning: a survey, *Journal of Machine Learning Research* **18**, 1 (2018).
- [35] M. Abdelhafez, D. I. Schuster, and J. Koch, Gradient-based optimal control of open quantum systems using quantum trajectories and automatic differentiation, *Phys. Rev. A* **99**, 052327 (2019).
- [36] Y. Lu, S. Joshi, V. S. Dinh, and J. Koch, Optimal control of large quantum systems: assessing memory and runtime performance of GRAPE, *arXiv* (2023), 2304.06200.
- [37] L. Pontryagin, V. Boltyanskii, R. Gamkrelidze, and E. Mishechenko, *The Mathematical Theory of Optimal Processes* (CRC Press, 1962).
- [38] N. B. Dehaghani and A. P. Aguiar, An application of pontryagin neural networks to solve optimal quantum control problems, *arXiv preprint* (2023), 2302.09143.
- [39] U. Boscain, M. Sigalotti, and D. Sugny, Introduction to the pontryagin maximum principle for quantum optimal control, *PRX Quantum* **2**, 030203 (2021).
- [40] R. T. Chen, Y. Rubanova, J. Bettencourt, and D. K. Duvenaud, Neural ordinary differential equations, *Advances in neural information processing systems* **31** (2018).
- [41] P. Kidger, *On neural differential equations*, Ph.D. thesis, Mathematical Institute, University of Oxford (2022), 2202.02435.
- [42] J. Somló, V. A. Kazakov, and D. J. Tannor, Controlled dissociation of i2 via optical transitions between the x and b electronic states, *Chemical physics* **172**, 85 (1993).
- [43] M. H. Goerz, S. C. Carrasco, and V. S. Malinovsky, Quantum optimal control via semi-automatic differentiation, *Quantum* **6**, 871 (2022).
- [44] S. H. K. Narayanan, T. Propson, M. Bongarti, J. Hückelheim, and P. Hovland, Reducing memory requirements of quantum optimal control, in *International Conference on Computational Science* (Springer, 2022) pp. 129–142.
- [45] A. Blais, R.-S. Huang, A. Wallraff, S. M. Girvin, and R. J. Schoelkopf, Cavity quantum electrodynamics for superconducting electrical circuits: An architecture for quantum computation, *Phys. Rev. A* **69**, 062320 (2004).
- [46] T. Walter, P. Kurpiers, S. Gasparinetti, P. Magnard, A. Potočnik, Y. Salathé, M. Pechal, M. Mondal, M. Oppliger, C. Eichler, and A. Wallraff, Rapid high-fidelity single-shot dispersive readout of superconducting qubits, *Phys. Rev. Appl.* **7**, 054020 (2017).
- [47] Y. Sunada, S. Kono, J. Ives, S. Tamate, T. Sugiyama, Y. Tabuchi, and Y. Nakamura, Fast readout and reset of a superconducting qubit coupled to a resonator with an intrinsic purcell filter, *Phys. Rev. Appl.* **17**, 044016 (2022).
- [48] M. Pechal, L. Huthmacher, C. Eichler, S. Zeytinoğlu, A. A. Abdumalikov, S. Berger, A. Wallraff, and S. Filipp, Microwave-controlled generation of shaped single photons in circuit quantum electrodynamics, *Phys. Rev. X*

- 4, 041010 (2014).
- [49] P. Magnard, P. Kurpiers, B. Royer, T. Walter, J.-C. Besse, S. Gasparinetti, M. Pechal, J. Heinsoo, S. Storz, A. Blais, and A. Wallraff, Fast and unconditional all-microwave reset of a superconducting qubit, *Phys. Rev. Lett.* **121**, 060502 (2018).
- [50] J. Koch, T. M. Yu, J. Gambetta, A. A. Houck, D. I. Schuster, J. Majer, A. Blais, M. H. Devoret, S. M. Girvin, and R. J. Schoelkopf, Charge-insensitive qubit design derived from the cooper pair box, *Phys. Rev. A* **76**, 042319 (2007).
- [51] C. Gardiner and P. Zoller, *Quantum noise: a handbook of Markovian and non-Markovian quantum stochastic methods with applications to quantum optics* (Springer Science & Business Media, 2004).
- [52] See Supplemental Material for more information.
- [53] C. G. Broyden, The convergence of a class of double-rank minimization algorithms 1. general considerations, *IMA Journal of Applied Mathematics* **6**, 76 (1970).
- [54] D. P. Kingma and J. Ba, Adam: A method for stochastic optimization, arXiv <https://doi.org/10.48550/arXiv.1412.6980> (2014), 1412.6980.
- [55] H. Robbins and S. Monro, A Stochastic Approximation Method, *The Annals of Mathematical Statistics* **22**, 400 (1951).
- [56] A. Paszke, S. Gross, F. Massa, A. Lerer, J. Bradbury, G. Chanan, T. Killeen, Z. Lin, N. Gimelshein, L. Antiga, *et al.*, Pytorch: An imperative style, high-performance deep learning library, *Advances in neural information processing systems* **32** (2019), 1912.01703.
- [57] P. Guilmin, R. Gautier, A. Bocquet, and E. Genois, dynamics: an open-source library for GPU-accelerated and differentiable simulation of quantum systems (2024), in preparation, library available at [dynamics.org](https://dynamics.org).
- [58] A. Blais, A. L. Grimsmo, S. M. Girvin, and A. Wallraff, Circuit quantum electrodynamics, *Rev. Mod. Phys.* **93**, 025005 (2021).
- [59] J. Cohen, A. Petrescu, R. Shillito, and A. Blais, Reminiscence of classical chaos in driven transmons, *PRX Quantum* **4**, 020312 (2023).
- [60] R. Shillito, A. Petrescu, J. Cohen, J. Beall, M. Hauru, M. Ganahl, A. G. Lewis, G. Vidal, and A. Blais, Dynamics of transmon ionization, *Phys. Rev. Appl.* **18**, 034031 (2022).
- [61] M. F. Dumas, B. Groleau-Paré, A. McDonald, M. H. Muñoz-Arias, C. Lledó, B. D’Anjou, and A. Blais, Unified picture of measurement-induced ionization in the transmon (2024), arXiv:2402.06615.
- [62] F. Swiadek, R. Shillito, P. Magnard, A. Remm, C. Hellings, N. Lacroix, Q. Ficheux, D. C. Zanuz, G. J. Norris, A. Blais, *et al.*, Enhancing dispersive readout of superconducting qubits through dynamic control of the dispersive shift: Experiment and theory, arXiv (2023), 2307.07765.
- [63] C. C. Bultink, B. Tarasinski, N. Haandbæk, S. Poletto, N. Haider, D. Michalak, A. Bruno, and L. DiCarlo, General method for extracting the quantum efficiency of dispersive qubit readout in circuit qed, *Applied Physics Letters* **112**, <https://doi.org/10.1063/1.5015954> (2018).
- [64] J. Gambetta, W. A. Braff, A. Wallraff, S. M. Girvin, and R. J. Schoelkopf, Protocols for optimal readout of qubits using a continuous quantum nondemolition measurement, *Phys. Rev. A* **76**, 012325 (2007).
- [65] F. Motzoi, J. M. Gambetta, S. T. Merkel, and F. K. Wilhelm, Optimal control methods for rapidly time-varying hamiltonians, *Phys. Rev. A* **84**, 022307 (2011).
- [66] Y. Sunada, K. Yuki, Z. Wang, T. Miyamura, J. Ilves, K. Matsuura, P. A. Spring, S. Tamate, S. Kono, and Y. Nakamura, Photon-noise-tolerant dispersive readout of a superconducting qubit using a nonlinear purcell filter, *PRX Quantum* **5**, 010307 (2024).
- [67] J. Ikonen, J. Goetz, J. Ilves, A. Keränen, A. M. Gunyho, M. Partanen, K. Y. Tan, D. Hazra, L. Grönberg, V. Vesterinen, S. Simbierowicz, J. Hassel, and M. Möttönen, Qubit measurement by multichannel driving, *Phys. Rev. Lett.* **122**, 080503 (2019).
- [68] S. Touzard, A. Kou, N. E. Frattini, V. V. Sivak, S. Puri, A. Grimm, L. Frunzio, S. Shankar, and M. H. Devoret, Gated conditional displacement readout of superconducting qubits, *Phys. Rev. Lett.* **122**, 080502 (2019).
- [69] M. H. Muñoz Arias, C. Lledó, and A. Blais, Qubit readout enabled by qubit cloaking, *Phys. Rev. Appl.* **20**, 054013 (2023).
- [70] F. Mallet, F. R. Ong, A. Palacios-Laloy, F. Nguyen, P. Bertet, D. Vion, and D. Esteve, Single-shot qubit readout in circuit quantum electrodynamics, *Nat Phys* **5**, 791 (2009).
- [71] B. D’Anjou and W. A. Coish, Enhancing qubit readout through dissipative sub-poissonian dynamics, *Phys. Rev. A* **96**, 052321 (2017).
- [72] S. S. Elder, C. S. Wang, P. Reinhold, C. T. Hann, K. S. Chou, B. J. Lester, S. Rosenblum, L. Frunzio, L. Jiang, and R. J. Schoelkopf, High-fidelity measurement of qubits encoded in multilevel superconducting circuits, *Phys. Rev. X* **10**, 011001 (2020).
- [73] L. Chen, H.-X. Li, Y. Lu, C. W. Warren, C. J. Križan, S. Kosen, M. Rommel, S. Ahmed, A. Osman, J. Biznárová, *et al.*, Transmon qubit readout fidelity at the threshold for quantum error correction without a quantum-limited amplifier, *npj Quantum Information* **9**, 26 (2023).
- [74] S. Zeytinoglu, M. Pechal, S. Berger, A. A. Abdumalikov, A. Wallraff, and S. Filipp, Microwave-induced amplitude- and phase-tunable qubit-resonator coupling in circuit quantum electrodynamics, *Phys. Rev. A* **91**, 043846 (2015).
- [75] J. F. Poyatos, J. I. Cirac, and P. Zoller, Quantum reservoir engineering with laser cooled trapped ions, *Phys. Rev. Lett.* **77**, 4728 (1996).
- [76] P. M. Harrington, E. Mueller, and K. Murch, Engineered dissipation for quantum information science (2022), arXiv:2202.05280 [quant-ph].
- [77] B. Royer, S. Singh, and S. M. Girvin, Stabilization of finite-energy gottesman-kitaev-preskill states, *Phys. Rev. Lett.* **125**, 260509 (2020).
- [78] J. M. Gertler, B. Baker, J. Li, S. Shirol, J. Koch, and C. Wang, Protecting a bosonic qubit with autonomous quantum error correction, *Nature* **590**, 243–248 (2021).
- [79] P. Aliferis and B. M. Terhal, Fault-tolerant quantum computation for local leakage faults, *Quantum Info. Comput.* **7**, 139–156 (2007).

# Supplemental Material for "Optimal control in large open quantum systems – the case of transmon readout and reset"

Ronan Gautier,<sup>1,2,3</sup> Élie Genois,<sup>1</sup> and Alexandre Blais<sup>1,4</sup>

<sup>1</sup>*Institut Quantique and Département de Physique,  
Université de Sherbrooke, Sherbrooke, QC, Canada*

<sup>2</sup>*Laboratoire de Physique de l'École Normale Supérieure, Inria, ENS,  
Mines ParisTech, Université PSL, Sorbonne Université, Paris, France*

<sup>3</sup>*Alice & Bob, Paris, France*

<sup>4</sup>*Canadian Institute for Advanced Research, Toronto, ON, Canada*

## CONTENTS

S1. Adjoint state method for open quantum systems	1
A. Adjoint state master equation	1
B. Explicit expression of gradients	1
C. Practical implementation	2
S2. Optimal control of a transmon	2
A. Optimization process	2
B. Numerical integration scheme	3
C. Gaussian filtering	3
D. Cost function contributions	3
S3. Transmon readout	4
A. Assignment error	4
B. Phase-space trajectories	5
S4. Transmon reset	5
A. Calibration	5
B. Pulses	5

## S1. ADJOINT STATE METHOD FOR OPEN QUANTUM SYSTEMS

### A. Adjoint state master equation

In this section, we prove that the adjoint state follows the differential equation shown in the main text, following a similar derivation as in Ref. [1]. Starting from a general Lindblad master equation

$$\frac{d\hat{\rho}}{dt} = \mathcal{L}\hat{\rho} \equiv -i[\hat{H}, \hat{\rho}] + \sum_k \mathcal{D}[\hat{L}_k]\hat{\rho}, \quad (\text{S1})$$

we can write that for an  $\varepsilon$  change in time, the evolved quantum state takes the form

$$\begin{aligned} \hat{\rho}(t + \varepsilon) &= \hat{\rho}(t) + \int_t^{t+\varepsilon} \mathcal{L}(\tau, \theta)\hat{\rho}(\tau)d\tau \\ &= \hat{\rho}(t) + \varepsilon\mathcal{L}(t, \theta)\hat{\rho}(t) + \mathcal{O}(\varepsilon^2). \end{aligned} \quad (\text{S2})$$

Using the definition of the adjoint state and applying the chain rule, we find

$$\begin{aligned} \hat{\phi}(t) &= \frac{dC}{d\hat{\rho}(t)} = \frac{dC}{d\hat{\rho}(t + \varepsilon)} \frac{d\hat{\rho}(t + \varepsilon)}{d\hat{\rho}(t)} \\ &= \hat{\phi}(t + \varepsilon) (1 + \varepsilon\mathcal{L}(t, \theta) + \mathcal{O}(\varepsilon^2)). \end{aligned} \quad (\text{S3})$$

Then, the proof of the adjoint state master equation follows directly from the definition of the derivative,

$$\begin{aligned} \frac{d\hat{\phi}(t)}{dt} &= \lim_{\varepsilon \rightarrow 0} \frac{\hat{\phi}(t + \varepsilon) - \hat{\phi}(t)}{\varepsilon} \\ &= -\lim_{\varepsilon \rightarrow 0} \left( \hat{\phi}(t + \varepsilon)\mathcal{L}(t, \theta) + \mathcal{O}(\varepsilon^2) \right) \\ &= -\hat{\phi}(t)\mathcal{L}(t, \theta) \end{aligned} \quad (\text{S4})$$

or equivalently, using the fact that the adjoint state is hermitian,  $\hat{\phi}^\dagger = dC/d\hat{\rho}^\dagger = dC/d\hat{\rho} = \hat{\phi}$ , we get the following result thus completing the proof

$$\frac{d\hat{\phi}(t)}{dt} = -\mathcal{L}^\dagger(t, \theta)\hat{\phi}(t). \quad (\text{S5})$$

### B. Explicit expression of gradients

To derive an explicit expression for  $dC/d\theta$ , we also follow Ref. [1] and introduce an augmented density matrix  $\hat{\rho}_{aug}(t) = [\hat{\rho}(t), \theta(t)]^T$  which includes a second block row with time-dependent parameters. In practice, parameters are constant throughout the integration, but this fictitious time-dependence will allow us to isolate the sensitivity of the cost function to an infinitesimal change of parameters at each point in time. The augmented density matrix follows the differential equation

$$\frac{d\hat{\rho}_{aug}(t)}{dt} = \mathcal{L}_{aug}(t, \theta)\hat{\rho}_{aug}(t) = \begin{pmatrix} \mathcal{L}(t, \theta)\hat{\rho}(t) \\ 0 \end{pmatrix}. \quad (\text{S6})$$

We can also introduce the augmented adjoint state,  $\hat{\phi}_{aug}(t) = [\hat{\phi}(t), dC/d\theta(t)]$ , where the parameter sensitivity  $dC/d\theta(t)$  represents the cost function gradient with respect to the parameters at a given time. We then follow a similar derivation as in the previous section. The main difference comes in the application of the chain rule of Eq. (S3) which now yields,

$$\begin{aligned} \hat{\phi}_{aug}(t) &= \frac{dC}{d\hat{\rho}_{aug}(t)} = \frac{dC}{d\hat{\rho}_{aug}(t + \varepsilon)} \frac{d\hat{\rho}_{aug}(t + \varepsilon)}{d\hat{\rho}_{aug}(t)} \\ &= \hat{\phi}_{aug}(t + \varepsilon) (1 + \varepsilon\mathcal{M}(t, \theta) + \mathcal{O}(\varepsilon^2)) \end{aligned} \quad (\text{S7})$$

where

$$\begin{aligned} \mathcal{M}(t, \theta) &= \frac{d(\mathcal{L}_{aug}(t, \theta)\hat{\rho}_{aug}(t))}{d\hat{\rho}_{aug}(t)} \\ &= \begin{pmatrix} \mathcal{L}(t, \theta) & \partial_\theta \mathcal{L}(t, \theta)\hat{\rho}(t) \\ 0 & 0 \end{pmatrix}, \end{aligned} \quad (\text{S8})$$

and where  $\partial_\theta$  denotes the partial derivative with respect to  $\theta$ . Similarly as before, we can rearrange this expression, reinsert it in the definition of the derivative and take the limit of  $\varepsilon \rightarrow 0$ . Then, selecting only the second block of the resulting differential equation yields

$$\frac{d}{dt} \left( \frac{dC}{d\theta(t)} \right) = -\partial_\theta \text{Tr} \left[ \hat{\phi}^\dagger(t) \mathcal{L}(t, \theta) \hat{\rho}(t) \right]. \quad (\text{S9})$$

We have thus obtained a straightforward differential equation on the parameter sensitivity. Integrating this equation from  $t = 0$  to  $T$ , with the initial condition that  $dC/d\theta(T) = \partial C/\partial\theta$  yields

$$\frac{dC}{d\theta} = \frac{\partial C}{\partial\theta} - \int_T^0 \partial_\theta \text{Tr} \left[ \left( \mathcal{L}^\dagger(t, \theta) \hat{\phi}(t) \right) \hat{\rho}(t) \right] dt, \quad (\text{S10})$$

which is Eq. (3) in the main text. We can also get the derivative of the loss function with respect to the integration time  $T$  from a simple application of the chain rule

$$\frac{dC}{dT} = \frac{dC}{d\hat{\rho}(T)} \frac{d\hat{\rho}(T)}{dT} = \text{Tr} \left[ \hat{\phi}^\dagger(T) \mathcal{L}(T, \theta) \hat{\rho}(T) \right]. \quad (\text{S11})$$

Finally, between Eqs. (S5), (S10) and (S11), we obtain the gradients of the loss function with respect to all relevant objects involved in the computation, thus allowing one to perform gradient descent for the desired parameters from arbitrary cost functions.

### C. Practical implementation

The full implementation in Python of the approach described in the main text is available on the freely available open-source software `dynamics` [2]. To summarize the structure of a numerical implementation of the adjoint state method for open quantum systems, we present a pseudo-code implementation in Alg. 1. It involves a function `ODEstep(f, t, y, theta)` that computes a single step of the integration of a linear ordinary differential equation,  $\dot{y} = f(t, \theta)y$ , at time  $t$ . The `CostFn(theta, L_rho)` function computes the cost function from the parameters  $\theta$  and a list of density matrices  $L_\rho$ . It can also be computed on the fly in the `for` loop to avoid storing these matrices. Finally, the `AutoDiff(g, x_out, x_in)` function computes the partial derivative  $\partial x_{out}/\partial x_{in}$  through automatic differentiation of  $g$ , where  $x_{in}$  and  $x_{out}$  are given inputs and outputs of the function  $g$ . Note that lines 17 and 18 can be merged in a single computation of a vector-Jacobian product to avoid storage of  $\delta\phi$ .

---

### Algorithm 1: Adjoint state method for open quantum systems.

---

```

1  $t \leftarrow t_0$ ;
2  $\rho \leftarrow \rho_0$ ;
3  $L_\rho \leftarrow \{\rho_0\}$ ; // checkpoint storage list (optional)
4 for  $t_i \in \{t_1, \dots, t_n\}$  do // forward pass
5   while  $t < t_i$  do
6      $\rho, \delta t \leftarrow \text{ODEstep}(\mathcal{L}, t, \rho, \theta)$ ;
7      $t \leftarrow t + \delta t$ 
8   end
9    $L_\rho \leftarrow L_\rho + \{\rho\}$ ;
10 end
11  $C \leftarrow \text{CostFn}(\theta, L_\rho)$ ;
12  $\phi \leftarrow \text{AutoDiff}(\text{CostFn}, C, L_\rho[n])$ ;
13  $\nabla \leftarrow \text{AutoDiff}(\text{CostFn}, C, \theta)$ ;
14 for  $t_i \in \{t_{n-1}, \dots, t_0\}$  do // backward pass
15   while  $t > t_i$  do
16      $\{\rho, \phi\}, \delta t \leftarrow \text{ODEstep}(\{-\mathcal{L}, \mathcal{L}^\dagger\}, t, \{\rho, \phi\}, \theta)$ ;
17      $\delta\phi \leftarrow \text{AutoDiff}(\text{ODEstep}, \phi, \theta)$ ;
18      $\nabla \leftarrow \nabla - \text{Tr}[\delta\phi \cdot \rho]$ ;
19      $t \leftarrow t - \delta t$ ;
20   end
21    $\phi \leftarrow \phi + \text{AutoDiff}(\text{CostFn}, C, L_\rho[i])$ ;
22    $\rho \leftarrow L_\rho[i]$ ;
23 end
24 return  $\nabla$ 

```

---

## S2. OPTIMAL CONTROL OF A TRANSMON

### A. Optimization process

In this work, we optimize transmon readout and reset by simulating the Lindblad master equation of Eq. (S1) with the Hamiltonian of the main text which contains three modes: the full transmon Hamiltonian, a readout resonator and a Purcell filter. In our simulations, we first diagonalize the transmon Hamiltonian in the charge basis using 300 charge states and then truncate the subsystem to  $N_t = 5$  eigenstates of lowest energy. In parallel, we also diagonalize the resonator-filter subsystem yielding two normal modes – each coupled to the transmon – and keep  $N_d$  Fock states for the mode used to readout/reset the transmon (driven mode) and  $N_u$  Fock states in the other mode (undriven mode). For readout, we typically take  $N_d = 85$  and  $N_u = 4$ . For reset, we instead use  $N_d = N_u = 4$  since neither mode is actively driven.

Note that we intentionally select small Hilbert space sizes to lower the simulation runtime: a typical gradient descent on such transmon readout/reset simulations takes a few days per data point using a single GPU [3]. To avoid probing unphysical simulations with such low Hilbert space sizes, we actively steer the optimizer in two ways. First, we engineer the cost function such as to avoid large populations in boundary Fock states and limit the pulse amplitudes. See Table I for detailed cost function contributions. Second, we validate all optimized simulations with a single additional simulation in

Description	Analytical formula	Weight	Hyperparameters
Signal-to-noise ratio	$1/\sqrt{2\eta\kappa} \int_0^{\tau_m}  \beta_e(t) - \beta_g(t) ^2 dt$	1	$\eta = 0.6, \kappa/2\pi = 30$ MHz
Pulse amplitude (filter)	$\frac{1}{\tau_m} \int_0^{\tau_m} \text{ReLU}( \Omega_f(t)  - \Omega_{\max}) dt$	0.1	$\Omega_{\max}/2\pi = 200$ MHz
Pulse amplitude (transmon)	$\frac{1}{\tau_m} \int_0^{\tau_m} \text{ReLU}( \Omega_t(t)  - \Omega_{\max}) dt$	0.1	$\Omega_{\max}/2\pi = 200$ MHz
Forbidden states (transmon)	$\sum_{i=g,e} \sum_{k \geq n}^{N_t-1} \frac{1}{\tau_m} \int_0^{\tau_m} \text{Tr} [ k\rangle\langle k _t \hat{\rho}_i(t)] dt$	1.0	$n = 2$ or $3, N_t = 5$
Forbidden states (undriven normal)	$\sum_{i=g,e} \sum_{k \geq n}^{N_u-1} \frac{1}{\tau_m} \int_0^{\tau_m} \text{Tr} [ k\rangle\langle k _u \hat{\rho}_i(t)] dt$	5000	$n = 2, N_u = 4$
Critical photon number (resonator)	$\sum_{i=g,e} \frac{1}{\tau_m} \int_0^{\tau_m} \text{ReLU}(\text{Tr} [\hat{a}^\dagger \hat{a} \hat{\rho}_i(t)] - \bar{n}_{\text{crit}}) dt$	0.1	$\bar{n}_{\text{crit}} = 16$
State reset $ g\rangle$	$\log_{10}(1 -  \langle g00   \hat{\rho}_g(\tau_m)   g00 \rangle ^2)$	0.3	–
State reset $ e\rangle$	$\log_{10}(1 -  \langle g00   \hat{\rho}_e(\tau_m)   g00 \rangle ^2)$	1.0	–
State reset $ f\rangle$	$\log_{10}(1 -  \langle g00   \hat{\rho}_f(\tau_m)   g00 \rangle ^2)$	0.3	–
Pulse amplitude (transmon)	$\frac{1}{\tau_m} \int_0^{\tau_m} \text{ReLU}( \Omega_t(t)  - \Omega_{\max}) dt$	0.1	$\Omega_{\max}/2\pi = 600$ MHz

Table I. Summary of readout (top) and reset (bottom) cost functions. Each line corresponds to a different contribution to the total cost function, with an overall weight tuned heuristically. All contributions are functions of the problem parameters and/or of the density matrix at certain times. Time integrals are numerically discretized in 1 ns time bins. ReLU denotes a rectified linear unit function such that  $\text{ReLU}(x) = 0$  for  $x \leq 0$  and  $\text{ReLU}(x) = x$  for  $x \geq 0$ . The states  $|k\rangle_t$  and  $|k\rangle_u$  denote the  $k$ -th Fock state in the transmon and undriven normal mode respectively. Finally,  $\hat{\rho}_i$  denotes the density matrix for a transmon initialized in state  $|i\rangle_t$ .

a larger Hilbert space, using pulses as obtained by the optimization process. For such simulations, we typically take  $N_t = 6$ , and  $N_d = 90$  and  $N_u = 8$  for readout, or  $N_d = N_u = 8$  for reset. All data points shown in the main text correspond to such validated simulations, and do not deviate significantly from the results obtained on the reduced Hilbert space simulations.

## B. Numerical integration scheme

Regarding the integration scheme of the ordinary differential equation (ODE), we used a second-order Rouchon solver [4] with a fixed integration time step of  $\delta t = 0.003$  ns. Such a method ensures preservation of the positivity and trace of the density matrix at all times during the integration, contrary to standard ODE integration schemes. This is particularly interesting in the context of the adjoint state method to avoid divergence during the reverse-time integration of the master equation. Later on in this work, we have also used a standard order-4/5 Dormand-Prince integration scheme [5] which provided better runtimes in the forward pass and similar ones in the backward pass, even considering the stiffness of the reverse-time integration. In any case, several thousands of integration steps are typically required in our simulations. This makes the use of standard automatic differentiation prohibitive in computer memory. A simple pen-and-paper estimation of memory with the previously stated Hilbert space size and  $M_t = 10000$  time steps yields a memory footprint of  $8M_t(N_t N_d N_u)^2 = 215$  GB where 8 is the number of bytes used to store a single-precision complex number.

## C. Gaussian filtering

As stated in the main text, all simulated pulse envelopes are first discretized in  $\tau_0 = 1$  ns time bins and then gaussian filtered according to Ref. [6]. Each complex amplitude of the discretized pulse then corresponds to an additional parameter in the optimization. Concretely, the time-dependent pulses read

$$\Omega(t) = \mathcal{F}_g \left[ \sum_{j=0}^{\lfloor \tau_m/\tau_0 \rfloor - 1} \Omega_j \Pi_j(t, \tau_0) \right] (t) \quad (\text{S12})$$

where

$$\Pi_j(t, \tau_0) \equiv \Theta(t - j\tau_0) - \Theta(t - (j+1)\tau_0) \quad (\text{S13})$$

is the rectangle function, with  $\Theta$  is the Heaviside unit step function, and where  $\mathcal{F}_g$  is a gaussian filter of bandwidth  $\omega_B/2\pi = 250$  MHz. Commuting  $\mathcal{F}_g$  with the sum of Eq. (S12), we get the simpler expression

$$\Omega(t) = \sum_{j=0}^{\lfloor \tau_m/\tau_0 \rfloor - 1} \Omega_j \zeta_j(t), \quad (\text{S14})$$

where

$$\zeta_j(t) = \frac{1}{2} \left[ \text{erf} \left( \omega_0 \frac{t - j\tau_0}{2} \right) - \text{erf} \left( \omega_0 \frac{t - (j+1)\tau_0}{2} \right) \right], \quad (\text{S15})$$

with erf the error function and  $\omega_0/2\pi = 425.5$  MHz [6].

## D. Cost function contributions

Designing appropriate cost functions is essential to obtain useful quantum optimal control results from numeri-

cal optimizations. In this work, we define composite cost functions with a principal component and several smaller regularizing contributions. The cost functions used for transmon readout and reset are summarized in Table I. Let us describe each cost function separately.

For transmon readout, the main contribution is the inverse of the SNR. We use the inverse (instead of e.g. the negation) such that the optimizer focuses on other cost function contributions increasingly more as the SNR grows large. There are five regularizing cost functions on top of this main component. The first two correspond to a maximum pulse amplitude on the filter and transmon respectively, at  $\Omega_{max}/2\pi = 200$  MHz. These cost functions use a rectified linear unit function, or ReLU, such that  $\text{ReLU}(x) = 0$  for  $x \leq 0$  and  $\text{ReLU}(x) = x$  for  $x \geq 0$ . As such, no hard limits are set on the pulse amplitudes to allow the optimizer to explore a larger parameter space in case interesting solutions can be found at larger amplitudes. Two other contributions correspond to forbidden states in the transmon and undriven normal mode respectively. As previously discussed, these costs are used to avoid probing unphysical pulses that would make use of boundary Fock states sitting close to our artificial numerical truncation. Finally, the last contribution to the cost function is a soft upper bound on the number of photons in the resonator. Indeed, according to the standard theory of dispersive qubit readout [7], non-QND readout can be probed by driving the readout resonator above its critical number of photons  $\bar{n}_{crit}$ . This cost function also allows for a fair comparison between all readout strategies by limiting the effective speed of pointer state separation, given by  $\bar{n}\chi$  in the absence of additional transmon drives.

For transmon reset, the main contributions are the logarithms of residual population outside the  $|g00\rangle\langle g00|$  subspace, for a transmon initialized in either  $|g\rangle$ ,  $|e\rangle$ , or  $|f\rangle$ . In particular, we weight these three contributions non-uniformly with a larger weight on the  $|e\rangle$  state reset. This is a choice motivated by experimental designs for which population inside the qubit subspace is typically much larger than leaked population at the beginning of resets. However, these weights can be freely adapted to the experiment. The only regularizing cost function for transmon reset is an upper bound on the pulse amplitude, similar to that of transmon readout. Because reset attempts to evacuate the system photons, additional cost functions are not required.

In Fig. S1, we show how typical cost function contributions evolve as a function of the optimization epoch (i.e. iteration). Panel (a) shows a 40 ns transmon readout optimization where only the filter is driven, while panel (b) shows a 200 ns reset optimization. In both cases, we find a clear decrease in the total cost in the first 20 to 50 epochs, and convergence to a steady value afterwards. For readout, the cost function is dominated by the SNR cost function. The inset highlights the smaller cost contributions in log scale. For these regularizing cost functions, we regularly see peaks indicating that the op-

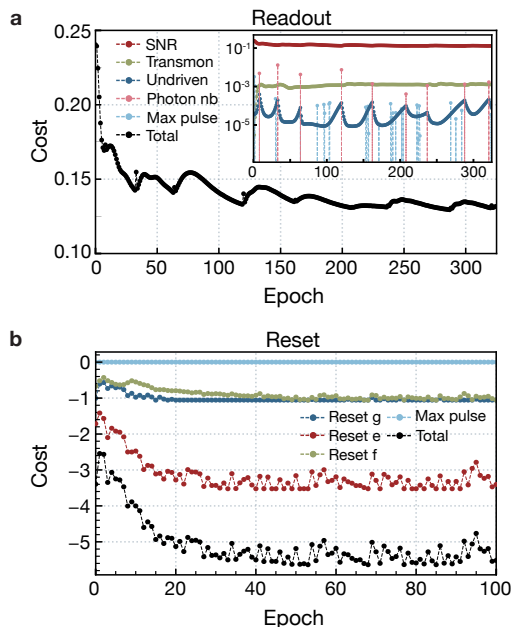


Figure S1. Cost function as a function of the optimization epoch for (a) transmon readout QOC with no transmon drive at 40 ns, and (b) transmon reset QOC at 200 ns. The inset of panel (a) shows the cost function contributions in log scale, with the main contribution being the inversed SNR. Other contributions are meant to regularize the pulse and to avoid unphysical regions. See Table I for the detailed cost function contributions.

imizer is generating dynamics close to the Hilbert space boundaries before retracting away, all the while achieving increasingly better SNR.

### S3. TRANSMON READOUT

#### A. Assignment error

In Fig. 2(c) of the main text, we show the assignment error of transmon readout as a function of the integration time. This assignment error is computed in Refs. [8, 9] assuming that the transmon pointer states stay gaussian during readout. This assumption is verified to a very good approximation for all of our simulated readout sequences. Given this structure, the assignment error reads

$$\varepsilon_a(\tau_m) \simeq \frac{1}{2} \operatorname{erfc} \left( \frac{\operatorname{SNR}(\tau_m)}{2} \right) + \frac{\tau_m}{2T_1}, \quad (\text{S16})$$

where  $\varepsilon_a = 1 - \mathcal{F} = [P(e|g) + P(g|e)]/2$ , with  $P(i|j)$  the probability of measuring state  $|i\rangle$  when  $|j\rangle$  is prepared,  $\mathcal{F}$  the readout fidelity, and  $\operatorname{erfc}$  the complementary error function.

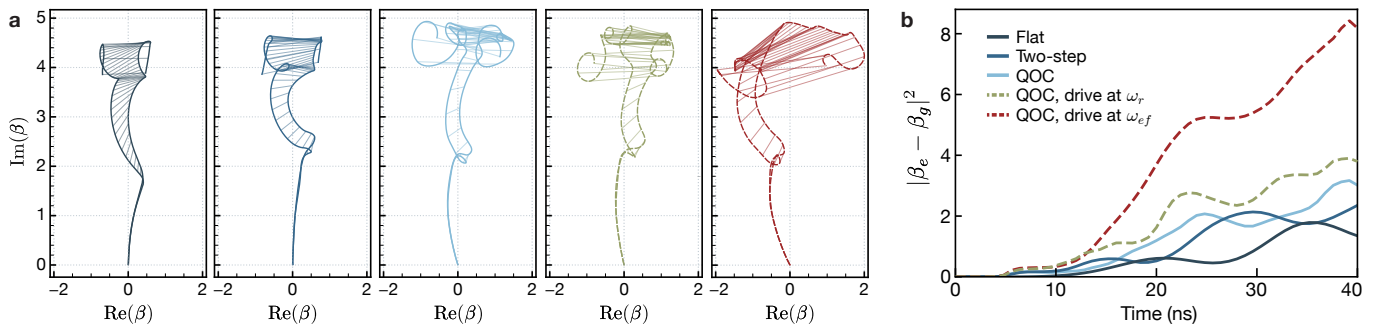


Figure S2. (a) Mean phase-space trajectories of the Purcell filter during a 40 ns readout. Each panel shows  $\beta_e$  and  $\beta_g$  against time for a different readout strategy, where  $\beta_{e/g} = \text{Tr}[\hat{f}\hat{\rho}_{g/e}]$  is the filter mean field after initializing the transmon in the  $|e\rangle$  or  $|g\rangle$  state. Lines that join each trajectory represent 1 ns intervals. The optimal control algorithm attempts to maximize SNR, which corresponds to the integrated distance between both trajectories. (b) Phase-space distance against time for the same readout strategies as in (a).

## B. Phase-space trajectories

Figure S2(a) shows the readout trajectories obtained by our three optimized control strategies, in comparison with the flat and two-step readout references. Notably, we see that pulse shaping the microwave drives on the cavity and qubit, while still using an experimentally-realistic bandwidth, makes the readout dynamics deviate from the usual dispersive trajectories. As quantified in Fig. S2(b), optimizing the control drives leads to both a faster and a larger separation between the qubit pointer states, which directly translates into better readout SNR. The red curve, which corresponds to adding the transmon drive at the  $|e\rangle$ - $|f\rangle$  transition frequency such as to achieve shelving, shows how beneficial that approach is for the system parameters considered here, compared to standard dispersive readout. The discovered scheme of simultaneously shelving and populating the readout mode with photons could straightforwardly be implemented with the typical controls available in current transmon experiments.

## S4. TRANSMON RESET

### A. Calibration

Since the f0-g1 reset of the transmon  $|e\rangle$  and  $|f\rangle$  states requires two concurrent microwave drives on the transmon, the frequency and amplitude of these drives need to be calibrated in a self-consistent way. In order to get the best reset performance using flat drives on which to compare our optimal controls, we perform a numerical calibration procedure that follows closely what is done in typical experiments [10, 11].

Namely, for a given f0-g1 drive amplitude  $\Omega_{f0g1}$ , we first scan the reset drive frequency  $\omega_{f0g1}$  to find the ac-Stark shifted resonant frequency that maps the prepared  $|f\rangle$  transmon state back to  $|g\rangle$  after 100 ns. The results of this simulated experiment are illustrated in Fig. S3(a,

e) for the lower and higher normal readout mode, respectively, and for different drive amplitudes  $\Omega_{f0g1}/2\pi$  between 50 and 650 MHz. Once the frequency  $\omega_{f0g1}$  is fixed on resonance, we calibrate the  $|e\rangle$ - $|f\rangle$  drive frequency  $\omega_{ef}$ . This is achieved by performing a similar experiment as before, but in which the transmon is prepared in  $|e\rangle$  instead of  $|f\rangle$ , and both the f0-g1 drive and e-f drives are on. The amplitude ratio  $\Omega_{f0g1}/\Omega_{ef}$  between both drives is kept constant such that the effective f0-g1 Rabi rate yields  $\tilde{g}(\Omega_{f0g1}) = \Omega_{ef}$  [11, 12]. The results of this second calibration are shown in Fig. S3(b, f) for the lower and higher modes, respectively. Finally, the  $|e\rangle$ - $|f\rangle$  drive amplitude  $\Omega_{ef}$  is calibrated from a 1D parameter sweep while performing the same  $|e\rangle$  reset experiment. This sweep is shown in Fig. S3(c, g). In the end, this whole procedure yields a single set of calibrated parameters ( $\omega_{f0g1}$ ,  $\omega_{ef}$ ,  $\Omega_{ef}$ ) for every value of  $\Omega_{f0g1}$  and for each normal mode. We simulate the corresponding reset of each set of calibrated parameters, and show the corresponding results in the panels of Fig. S3(d, h).

Out of all of the calibrated sets of parameters, we selected the best performing reset (both in terms of speed and fidelity) to compare with our optimal controls in Fig. 3 of the main text. This corresponds to a f0-g1 amplitude of  $\Omega_{f0g1}/2\pi = 350$  MHz driving the higher frequency normal mode of the coupled resonator-filter subsystem. This mode has a larger dispersive coupling to the transmon than the lower frequency normal mode. This particular reset is shown with a red title in Fig. S3(h).

### B. Pulses

In Fig. S4, we present the optimal reset pulse shapes found using our quantum optimal control approach. The 200 ns pulse of panel (b) produces the transmon population dynamics illustrated with the pink markers in Fig. 3 of the main text. Interestingly, in the 100 ns pulse of panel (a), we see that the numerical optimization yields an initial  $\pi$ -pulse to transfer population from  $|e\rangle$  to  $|f\rangle$

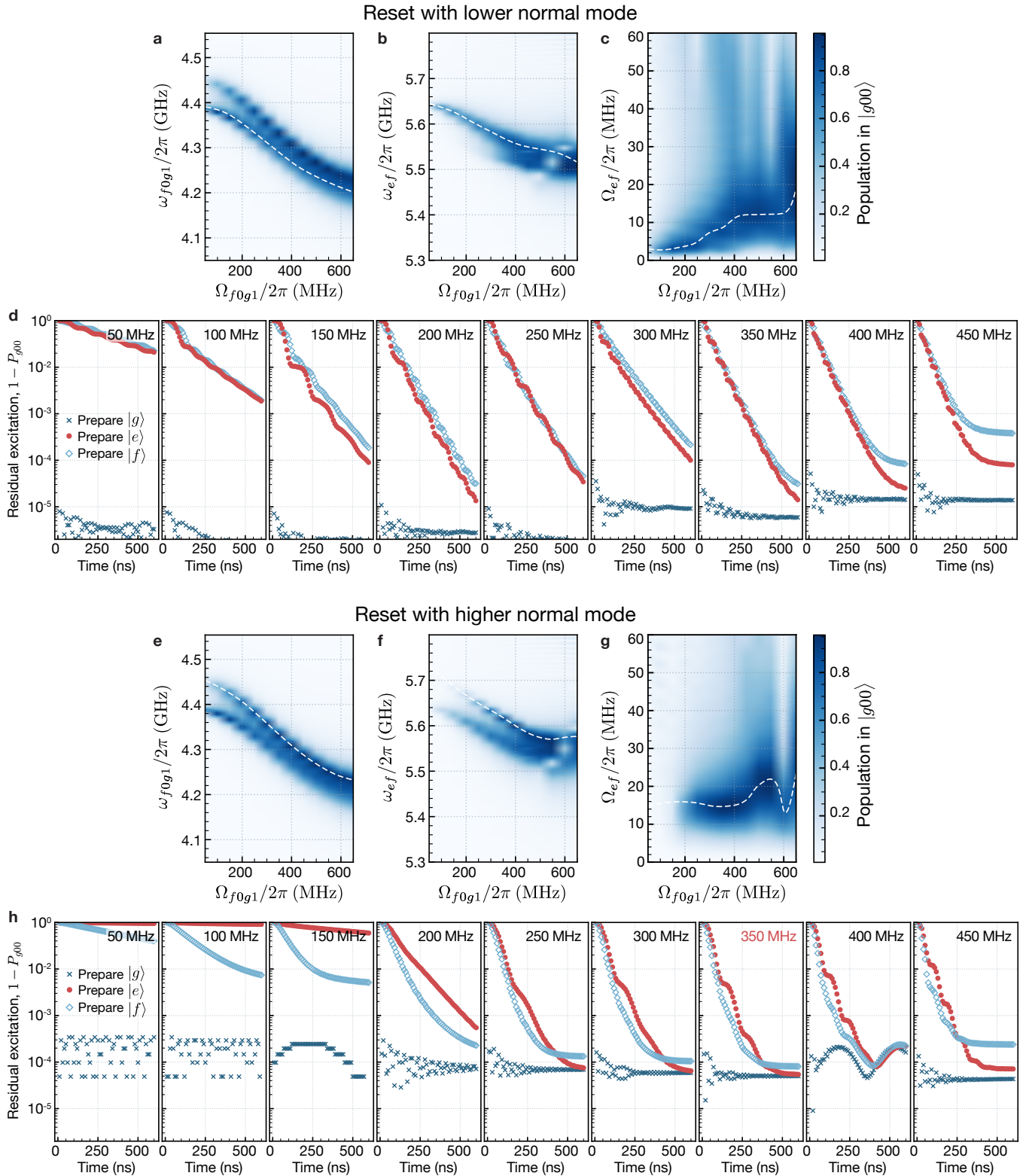


Figure S3. Numerical calibration of the f0-g1 reset for the reference flat drives. (a-c) Following the normal mode of lowest frequency, the f0-g1 drive frequency  $\omega_{f_0g_1}/2\pi$ , the e-f drive frequency  $\omega_{ef}/2\pi$ , and e-f drive amplitude  $\Omega_{ef}/2\pi$  are sequentially calibrated. See the protocol description in Sec. S4 for more details. (d) Resulting f0-g1 reset performance after preparing the  $|g\rangle$ ,  $|e\rangle$ , and  $|f\rangle$  states of the transmon for different f0-g1 drive amplitudes  $\Omega_{f_0g_1}/2\pi$  between 50 MHz and 450 MHz. (e-h) Results for the same calibration protocol, now following the normal readout mode with higher frequency. The selected reference f0-g1 reset for our system is highlighted in red and uses  $\Omega_{f_0g_1}/2\pi = 350$  MHz and the higher normal mode of the coupled resonator-filter subsystem.

which quickly decays back to  $|g\rangle$  because of the  $f_0$ - $g_1$  drive. This behaviour can be understood by the fact that our chosen cost function puts more weight into resetting the  $|e\rangle$  state. As such, the optimal drive scheme with this constraint initially resets the  $|e\rangle$  state, and subsequently resets the population that was initially in the  $|f\rangle$  state at the beginning of the protocol. This behaviour is consistent with the fact that the residual population when initializing in  $|e\rangle$  converges after 100 ns whereas it converges after 200 ns for the  $|f\rangle$  initial state, as reported in the main text. Our choice of relative weights between the different residual populations is motivated by the thermal population of a high frequency transmon (5 GHz) in a relatively cold environment (20 mK  $\sim$  417 MHz), but is arbitrary and could easily be adapted to other experimentally relevant scenarios, e.g. a low-frequency fluxonium qubit ( $<1$  GHz) in contact with the same thermal bath.

## REFERENCES

- [1] R. T. Chen, Y. Rubanova, J. Bettencourt, and D. K. Duvenaud, Neural ordinary differential equations, *Advances in neural information processing systems* **31** (2018).
- [2] P. Guilmin, R. Gautier, A. Bocquet, and E. Genois, dynamiqs: an open-source library for GPU-accelerated and differentiable simulation of quantum systems (2024), in preparation, library available at dynamiqs.org.
- [3] GPUs used: Nvidia RTX6000 24GB, Nvidia RTX8000 48GB, Nvidia V100 32GB, Nvidia RTX3080 10GB.
- [4] C. Le Bris and P. Rouchon, Low-rank numerical approximations for high-dimensional lindblad equations, *Phys. Rev. A* **87**, 022125 (2013).
- [5] J. R. Dormand and P. J. Prince, A family of embedded runge-kutta formulae, *Journal of computational and applied mathematics* **6**, 19 (1980).
- [6] F. Motzoi, J. M. Gambetta, S. T. Merkel, and F. K. Wilhelm, Optimal control methods for rapidly time-varying hamiltonians, *Phys. Rev. A* **84**, 022307 (2011).
- [7] A. Blais, A. L. Grimsmo, S. M. Girvin, and A. Wallraff, Circuit quantum electrodynamics, *Rev. Mod. Phys.* **93**, 025005 (2021).
- [8] J. Gambetta, W. A. Braff, A. Wallraff, S. M. Girvin, and R. J. Schoelkopf, Protocols for optimal readout of qubits using a continuous quantum nondemolition measurement, *Phys. Rev. A* **76**, 012325 (2007).
- [9] F. Swiadek, R. Shillito, P. Magnard, A. Remm, C. Hellings, N. Lacroix, Q. Ficheux, D. C. Zanuz, G. J. Norris, A. Blais, *et al.*, Enhancing dispersive readout of superconducting qubits through dynamic control of the dispersive shift: Experiment and theory, *arXiv* (2023), 2307.07765.
- [10] M. Pechal, L. Huthmacher, C. Eichler, S. Zeytinoglu, A. A. Abdumalikov, S. Berger, A. Wallraff, and S. Filipp, Microwave-controlled generation of shaped single photons in circuit quantum electrodynamics, *Phys. Rev. X* **4**, 041010 (2014).
- [11] P. Magnard, P. Kurpiers, B. Royer, T. Walter, J.-C. Besse, S. Gasparinetti, M. Pechal, J. Heinsoo, S. Storz, A. Blais, and A. Wallraff, Fast and unconditional all-microwave reset of a superconducting qubit, *Phys. Rev. Lett.* **121**, 060502 (2018).
- [12] S. Zeytinoglu, M. Pechal, S. Berger, A. A. Abdumalikov, A. Wallraff, and S. Filipp, Microwave-induced amplitude- and phase-tunable qubit-resonator coupling in circuit quantum electrodynamics, *Phys. Rev. A* **91**, 043846 (2015).

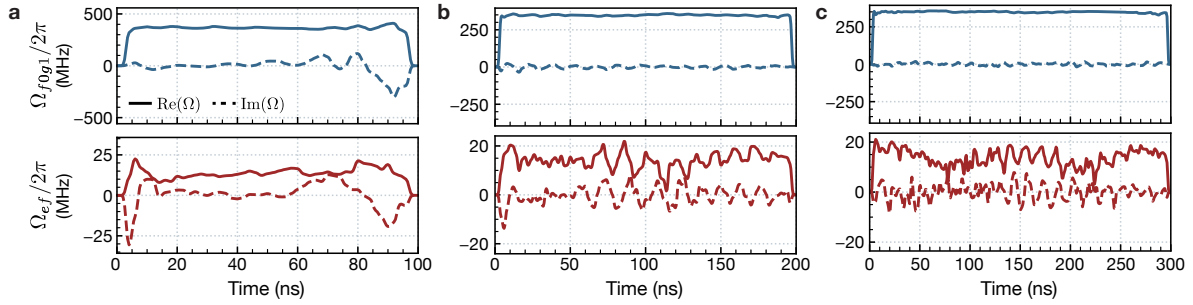


Figure S4. Optimal pulse shapes for reset durations of (a) 100 ns, (b) 200 ns, and (c) 300 ns. The f0-g1 drive  $\Omega_{f0g1}$  is illustrated in blue and the e-f drive  $\Omega_{ef}$  in red. Recall that although the features of  $\Omega_{ef}$  appear to be sharp, the pulses are filtered using an experimentally conservative gaussian filter with a bandwidth of 250 MHz, here and in all of our simulations. This realistic filtering makes these pulses easily implementable in practice.